Journal of Applied Geophysics 178 (2020) 104078

Contents lists available at ScienceDirect

Journal of Applied Geophysics

journal homepage: www.elsevier.com/locate/jappgeo

3D full-waveform inversion in time-frequency domain: Field data application

Khiem T. Tran [a,*], Trung Dung Nguyen [b], Dennis R. Hiltunen [a], Kenneth Stokoe [c], Farnyuh Menq [c]

[a] University of Florida, Department of Civil and Coastal Engineering, 365 Weil Hall, P.O. Box 116580, Gainesville, FL 32611, USA
[b] University of Canterbury, Christchurch, Canterbury, New Zealand
[c] University of Texas at Austin, Department of Civil, Architectural and Environmental Engineering, 301 E. Dean Keeton St. Stop C1700, Austin, TX 78712, USA

ARTICLE INFO

Article history:
Received 7 November 2019
Received in revised form 18 May 2020
Accepted 20 May 2020
Available online 23 May 2020

Keywords:
3D FWI
Anomaly detection
Gauss-Newton time-frequency inversion

ABSTRACT

We present a 3D Gauss-Newton full-waveform inversion (3D GN-FWI) method in the time-frequency domain for detection of subsurface anomalies. The use of Gauss-Newton approach is particularly important for near-surface imaging, in which acquired seismic wavefields are dominated by Rayleigh waves. The inverse Hessian matrix utilized in this approach acts as a weighting function to reduce the dominancy of Rayleigh waves, increase the contribution of body waves, and thus help resolve deeper structures. However, the Gauss-Newton method requires a huge amount of computer memory to store derivative wavefields (Jacobian matrix). To address this issue, the presented 3D GN-FWI method exploits advantages of the combined time-frequency domain. Specifically, the forward wave simulation is done in the time-domain to generate wavefields at multiple frequencies simultaneously without the requirement of an inverse matrix solver, while inversion is conducted in the frequency-domain to significantly reduce the required computer memory. Synthetic and field experimental datasets are used to assess the capability of the presented waveform method. The synthetic result shows that a variable profile with a buried void is well recovered. For the field experiment, a large mobile shaker was used to induce wavefields at individual frequencies with consistent magnitudes required for the presented frequency-domain inversion. The wavefields were recorded with uniform 2D grids of sources and receivers on the ground surface, and analyzed to obtain 3D subsurface wave velocity profiles. The seismic result is consistent with an invasive standard penetration test (SPT), including the identified bedrock depth and buried void.

1. Introduction

Unknown subsurface anomalies (*e.g.*, cavities, soft/weak zones, and buried objects) cause significant construction problems for many types of civil infrastructure (*e.g.*, roads, bridges, buildings, levees, tunnels). Non-invasive testing methods are often used for anomaly detection, as they can investigate subsurface conditions over a larger volume of materials at lower costs than invasive tests. Electromagnetic wave-based approaches, such as electrical resistivity and ground penetrating radar, have been routinely used for imaging of anomalies. However, identifying deep anomalies (>5–10 m depth) with these methods is often challenging (Wightman et al., 2003), and electromagnetic imaging cannot provide elastic properties that can be used in subsequent engineering analyses.

Seismic wave-based methods, including refraction tomography (Taillandier et al., 2009; Tran and Hiltunen, 2011) and surface wave approaches like multi-channel analysis of surface waves (MASW; Park et al., 1999), have also been used for anomaly detection (Tran and Hiltunen, 2012; Tran and Sperry, 2018). However, these methods only use a small percentage of the information in the waveform to infer subsurface properties, limiting their ability to detect variable subsurface conditions. For example, refraction methods only rely on the travel time of the fastest ray from a source to receivers. This is problematic for soft anomaly detection, as the fastest ray only travel through stiff materials and avoid soft anomalies. Surface wave approaches, such as pseudo-2D MASW, rely solely on the waveforms' dispersive components. Such methods result in averaged or smeared properties beneath the lateral extents of the array within the depth of about one wavelength. Larger array sizes and lower frequency/longer wavelengths are required when increasing the investigation depth, resulting in larger volumes of material being averaged, rendering them increasingly insensitive to deeper anomalies.

Full waveform inversion (FWI) methods are the most promising way to obtain true 3D subsurface seismic images for anomaly detection. The FWI approach has potential to produce more detailed subsurface information than conventional methods that use travel times or dispersion characteristics (Vireux and Operto, 2009). Significant progress on

---

[*] Corresponding author.
E-mail addresses: ttk@ufl.edu (K.T. Tran), andrei.nguyen@canterbury.ac.nz (T.D. Nguyen), dhilt@ce.ufl.edu (D.R. Hiltunen), k.stokoe@mail.utexas.edu (K. Stokoe), fymenq@utexas.edu (F. Menq).

https://doi.org/10.1016/j.jappgeo.2020.104078
0926-9851/

2D/3D FWI methodologies has been made in the last decade, from meters to kilometers depth. At kilometer-scales, several 3D FWI studies have been conducted on marine data (*e.g.*, acoustic FWI: Sirgue et al., 2010; Vigh et al., 2011; Plessix et al., 2013; Warner et al., 2013; Warner et al., 2013, Raknes et al., 2015, Marjanovíc et al., 2019; and elastic FWI: Prieux et al., 2013; Vigh et al., 2014; Marjanovíc et al., 2019). There have been also a few successful 3D FWI applications on field land seismic data (*e.g.*, acoustic FWI: Stopin et al., 2014; Sedova et al., 2017, and elastic FWI: Pérez Solano and Plessix, 2019). 3D FWI algorithms often use acoustic approximation due to computational challenges, and typically perform well for marine data. However, they are limited for land data due to ignorance of elastic effects (Butzer et al., 2013). For the land data, the acoustic approximation could be applicable to geological settings with smooth velocity transitions, but often causes significant inversion artifacts in case of geological settings with sharp velocity contrasts (Mora and Wu, 2018; Marjanovíc et al., 2019). As a result, the acoustic FWI is not efficient for detection of anomalies, which have sharp boundary contrasts. Studies on elastic 3D FWI at kilometer-scales (Prieux et al., 2013; Vigh et al., 2014; Marjanovíc et al., 2019; Pérez Solano and Plessix, 2019) are still rare.

At engineering scales (<30 m depth), there are significant challenges associated with FWI imaging. These challenges include: (1) the need for a powerful and consistent broadband energy source, (2) the dominancy of surface wave components, (3) significant variability of soil/rock lithology (Tran and Luke, 2017), (4) strong wave attenuation (Groos et al., 2014), 5) presence of irregular topography (Pan et al., 2018; Borisov et al., 2017), and 6) severe local solutions due to the presence of surface waves (Pérez Solano et al., 2014). They tend to create inversion artifacts and local solutions that, when coupled with the general complexity of FWI, have prevented these techniques from being employed on regular basis for near-surface imaging.

A few 3D FWI studies have been conducted for land seismic data at the engineering scales (*e.g.*, Fathi et al., 2016; Nguyen and Tran, 2018; Smith et al., 2018; Mirzanejad and Tran, 2019; Tran et al., 2019). The FWI techniques based on the gradient method often create substantial shallow artifacts. This is due to the dominancy of Rayleigh waves (high sensitivity at shallow depths), coupled with large residuals caused by source inconsistency, near-surface soil/rock variability, and irregular ground topography, leading to model overshooting (over fitting) at shallow depths. The artifacts limit the characterization depth.

To alleviate the problem, Tran et al. (2019) developed a time-domain 3D GN-FWI method to suppress inversion artifacts and improve characterized resolution with depth. The inverse Hessian matrix used in Gauss-Newton inversion balances the gradient vector and model update during inversion (Pratt et al., 1998; Sheen et al., 2006). It suppresses the dominance of Rayleigh waves (less weights for shallow cells where Rayleigh waves mostly passing) and increases the contribution of body waves (more weights for deeper cells where reflected/refracted body wave passing), and better resolves deep structures. As noted in Tran et al. (2019), applied to field experimental data and compared to results from a cross-adjoint 3D FWI (Nguyen and Tran, 2018), *Vs* profiles from the time-domain 3D GN-FWI are more consistent with subsurface data derived from the blow counts of invasive standard penetration test (SPT N-values).

The challenge of using the Gauss-Newton method is to calculate the inverse Hessian matrix, which requires intensive computer time and memory (RAM). At kilometer-scales, the inverse Hessian matrix are often approximated to mitigate the computer demands, such as the Gauss-Newton-Krylov (Akcelik et al., 2002), the coupled gradient and Newton (Epanomeritakis et al., 2008), the truncated Newton (Métivier et al., 2017), the pseudo Gauss-Newton (Pan et al., 2018) methods. At meter-scales, we use the complete inverse Hessian matrix to have full effects in filtering of the gradient and balancing the model update (Tran et al., 2019).

However, the time-domain Gauss-Newton inversion requires a large amount of computer RAM to store the Jacobian matrix, leading to limited number of cells and resolutions can be carried on standard computers. To address the issue, the time-domain 3D GN-FWI method (Tran et al., 2019) is extended to the time-frequency domain in this study. Specifically, the forward wave simulation is done in the time-domain, while inversion is conducted in the frequency-domain. The time-domain wavefields and Jacobian elements are stored for only at three frequencies (instead of thousands of time steps) to significantly reduce the required computer RAM. The assumption is that a few dominant frequency components could well represent waveforms for an entire filtered frequency bandwidth.

The capability of the presented time-frequency 3D GN-FWI algorithm was first verified with synthetic dataset generated from a realistic soil/rock profile with an embedded void. Then, it was applied to a Florida field experimental site for anomaly detection. A large mobile shaker was used to generate chirp wavefields at individual frequencies in the order of increasing frequencies. The wavefields were recorded continuously in the time-domain for all frequencies. The analyzed results are compared with an invasive SPT for assessment of the algorithm.

2. Implementation of 3D GN-FWI in Time-Frequency Domain

The time-domain 3D GN-FWI method (Tran et al., 2019) is extended to the time-frequency domain in this study. This combined time-frequency approach is based on a time-domain forward simulation, and a frequency-domain Gauss-Newton inversion to obtain subsurface material properties. 3D elastic wave equations are used for simulation of wave propagation. The time-domain staggered-grid finite-difference technique (Virieux, 1986) is used to solve these wave equations, with implementations of the free-surface condition (Robertsson, 1996) at the top boundary and the perfectly matched layer (PML) (Kamatitsch and Martin, 2007) at the vertical and bottom boundaries. See Nguyen and Tran (2018) for details.

3. Gauss-Newton inversion in the frequency-domain

To save the computer RAM, the inversion is conducted in the frequency-domain. Time-domain wavefields and Jacobian elements obtained from the forward wave simulation (one shot at a time) are converted into the frequency-domain. The time-domain components are replaced by those from the next shot simulation. The frequency-domain components (wavefields and Jacobian matrix) are stored for all shots at only three frequencies, instead of thousands of time steps. This reduces the required RAM by about 80%. Using the approach by Butzer et al. (2013) based on the discrete Fourier transformation, signals are converted from the time to frequency domain as:

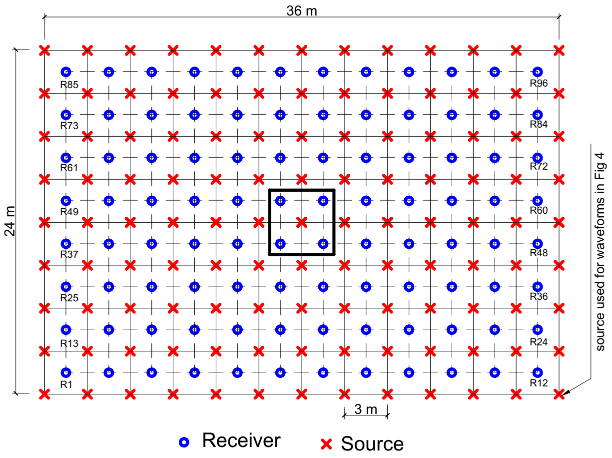

Fig. 1. Test configuration used for the synthetic experiment. The square box denotes a 4.5 m cube void burried at 9 m depth. Receiver numbers are noted as R1 to R96.

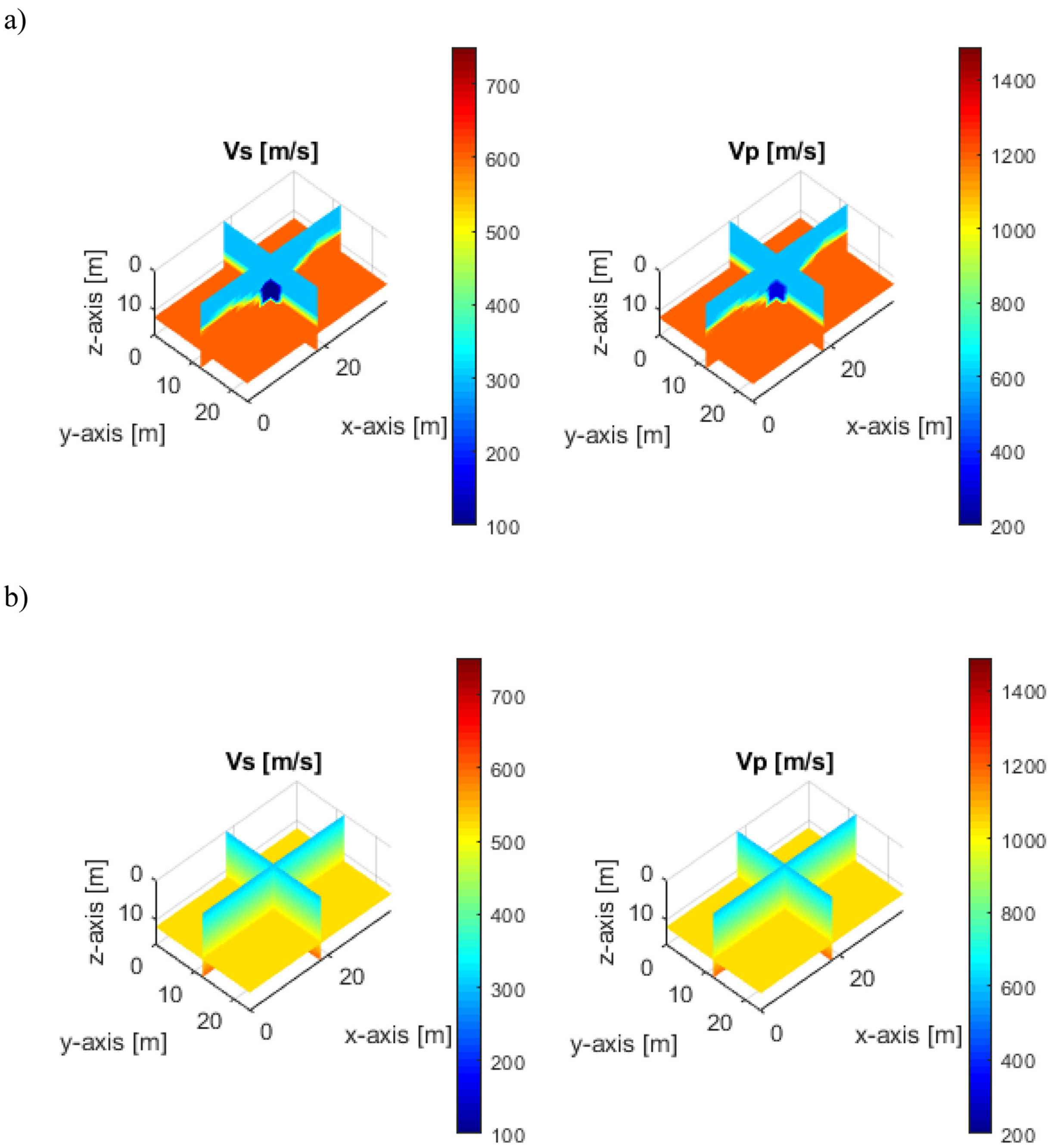

Fig. 2. Synthetic model: distribution of *Vs* and *Vp*: a) true model used to generate synthetic (observed) data for inversion analysis; b) initial model used at the beginning of inversion; c) final inverted result, d) velocity comparison for the vertical profile at the void center.

$$\tilde{u}(\mathbf{x},\omega)=\sum_{l=1}^{nt}\exp\left(\sqrt{-1}\omega l\Delta t\right)u(\mathbf{x},l\Delta t)\Delta t \tag{1}$$

where $\tilde{u}(\mathbf{x},\omega)$ is the frequency-domain signal for the sampled location $\mathbf{x}=(x,y,z)$ and frequency ω, $u(\mathbf{x}, l\Delta t)$ is the time domain signal and time $t=l\Delta t$, Δt is the time sampling, and nt is the number of time steps. The sampled location $\mathbf{x}$ are receivers for wavefield or cells for Jacobian components. Eq. (1) is used for all signals (estimated and measured wavefields, Jacobian matrix elements) in following Eqs. (2)–(4). Both real and imaginary components of the transformed signals are used.

The Gauss-Newton method minimizes the residual between estimated and observed (measured) waveform data, which is defined as:

$$\Delta\tilde{\boldsymbol{d}}_{s,r}=\tilde{\boldsymbol{F}}_{s,r}(\mathrm{m})-\tilde{\boldsymbol{d}}_{s,r} \tag{2}$$

where s and r denote the shot and receiver numbers, respectively. The vector $\tilde{\boldsymbol{F}}_{s,r}(\mathbf{m})$ is the frequency-domain estimated data associated with the model $\mathbf{m}$ (*Vs* and *Vp* of all cells), and obtained from the forward simulation. The vector $\tilde{\boldsymbol{d}}_{s,r}(\mathbf{m})$ is the frequency-domain observed waveform data for field testing.

The least-squares error $\mathrm{E}(\mathbf{m})$ is used for minimization of the residual as:

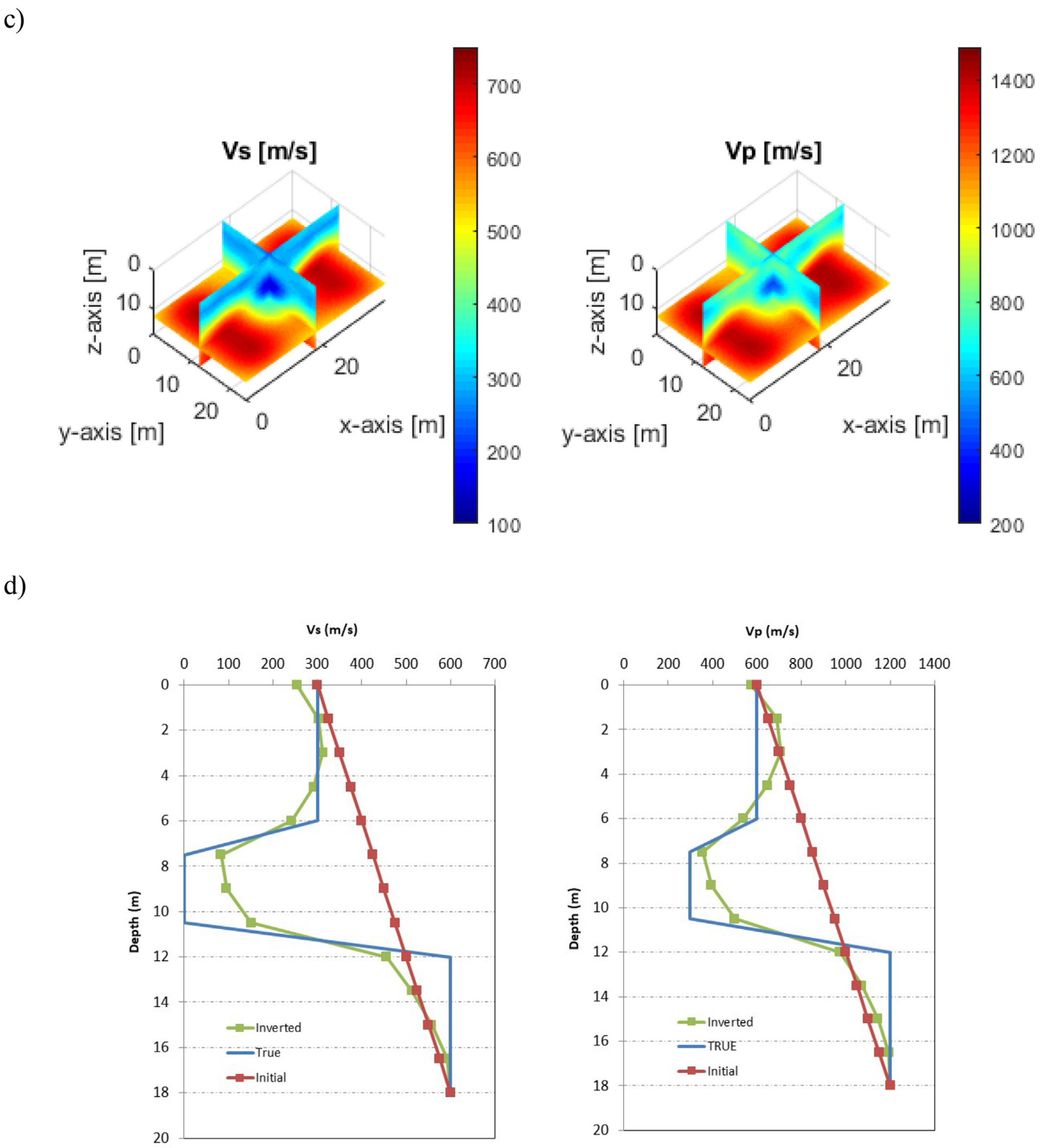

Fig. 2 (*continued*).

$$E(\mathbf{m}) = \frac{1}{2}\left\|\Delta\tilde{\mathbf{d}}\right\|^2 = \frac{1}{2}\Delta\tilde{\mathbf{d}}^t\Delta\tilde{\mathbf{d}},$$
$$\text{and } \Delta\tilde{\mathbf{d}} = \left\{\Delta\tilde{\mathbf{d}}_{s,r}, s = 1..NS, r = 1\ldots NR\right\} \tag{3}$$

where t denotes the matrix transpose, NS and NR are shot and receiver numbers, respectively. $\Delta\tilde{\mathbf{d}}$ is the residual for all shots and receivers, which are placed in a 2-D uniform grid on the ground surface. The size of the vector $\Delta\tilde{\mathbf{d}}_{s,r}$ is $2 \times NF \times NS \times NR$, where NF is the number of frequencies. The factor of 2 is for the real and imaginary components for each frequency.

By minimizing the error $E(\mathbf{m})$, the model $\mathbf{m}$ at iteration $(n + 1)$ is updated from the previous iteration as:

$$\mathbf{m}^{n+1} = \mathbf{m}^{n} - \alpha^{n}\left[\tilde{\mathbf{J}}^t\tilde{\mathbf{J}} + \lambda_1\mathbf{P}^t\mathbf{P} + \lambda_2\mathbf{I}^t\mathbf{I}\right]^{-1}\tilde{\mathbf{J}}^t\Delta\tilde{\mathbf{d}} \tag{4}$$

where the Jacobian matrix $\tilde{\mathbf{J}}$ is the frequency-domain partial derivative wavefield with respect to individual parameters (Vs and Vp of cells). The time-domain partial derivative wavefield $\mathbf{J}$ is calculated based on the convolution of the virtual source with reciprocal wavefields (Tran et al., 2019), and then converted to the frequency-domain $\tilde{\mathbf{J}}$. The number of forward simulations required for the calculation of Jacobian $\mathbf{J}$ is $NS + NR$. $\mathbf{I}$ is the identity matrix, and matrix $\mathbf{P}$ is determined via a 3D Laplacian operator with its elements of either 1, −6 or 0. Coefficients λ_1 and λ_2 are 0.02 and 0.0005 times of the maximum value of $\tilde{\mathbf{J}}^t\tilde{\mathbf{J}}$, respectively, as

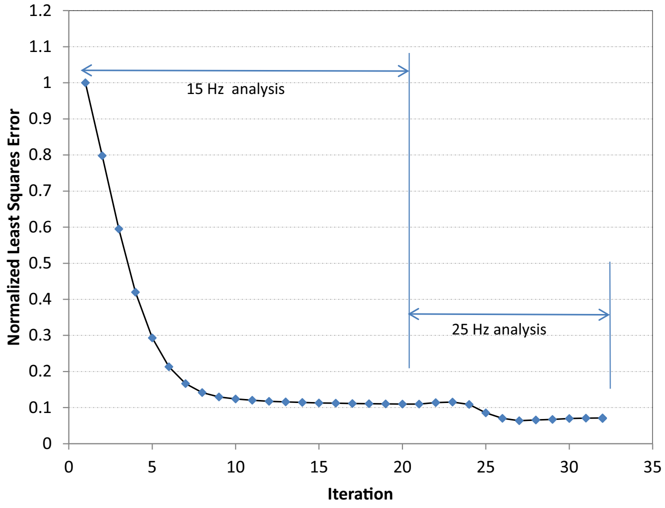

Fig. 3. Synthetic experiment: normalized least squares error *versus* the inversion iteration number for both inversion runs at 15 Hz and 25 Hz central frequencies. The error defines the degree of match between the estimated and observed waveforms during the inversion analysis.

suggested by Tran et al., 2019. The term ($\lambda_1 \mathbf{P}^t\mathbf{P} + \lambda_2 \mathbf{I}^t\mathbf{I}$) in Eq. (4) improves the invertability of the approximate Hessian matrix ($\mathbf{H_a} = \tilde{\mathbf{J}}^t\tilde{\mathbf{J}}$), and regularizes the inversion by constraining the model roughness (*e.g.* tying a cell to its six adjacent cells and larger λ_1 producing smoother models). The step length α^n is fixed at 1.0 in this study. See Tran et al. (2019) for details on the calculation of the time-domain $\mathbf{J}$.

4. Application on synthetic data

This section presents capability of the presented time-frequency 3D GN-FWI method for detection of buried anomaly. The method was tested on a realistic (synthetic) model of variable soil/rock layers with a buried void. Time-domain waveform data were simulated using 2D arrays of shots and receivers (Fig. 1). Then the data were analyzed by the 3D GN-FWI, as if they were field data. Inverted *Vs* and *Vp* are compared to their true values for assessment of the method capability.

The 18 × 36 × 24 m (depth × length × width) synthetic model consists of two variable layers with *Vs* of 300 m/s and 600 m/s, and *Vp* twice that of *Vs* (Fig. 2a). The blue cube is an air filled void of 4.5 m size with *Vs* of 0 m/s and *Vp* of 300 m/s, buried at 9 m (2 void sizes) depth (*e.g.* assigning $Vs = 0$ m/s and $Vp = 300$ m/s to all numerical nodes at the void location). The mass density is 1800 kg/m^3 for entire model. Synthetic waveform data were simulated via the 3D elastic wave solution (Nguyen and Tran, 2018). The medium was discretized into 1.5 × 1.5 × 1.5 m grid ($dh = 1.5$ m), and 10 grid points were added at the bottom and vertical boundaries for the perfectly matched layers. The time discretization was selected to satisfy the convergence criterion with the time step $dt \leq \frac{dh}{\sqrt{3}V_{p,max}}$. A Ricker wavelet of 15 Hz central frequency was used as the source signature for wave excitation. The test configuration includes 96 receivers and 117 sources, located in 8 × 12 and 9 × 13 grids respectively, both at 3 m spacing (Fig. 1).

This same synthetic dataset was filtered and used for two inversion runs with the central frequencies of 15 and 25 Hz. Instead of using only the central frequency (F_c) component for each run, two adjacent frequencies at ±20% of the central frequency (*e.g.* 0.8 F_c and 1.2 F_c) were also used to capture the filtered bandwidth (similar to Gaussian bell curve). The first run was at lower frequencies of 12, 15, and 18 Hz;

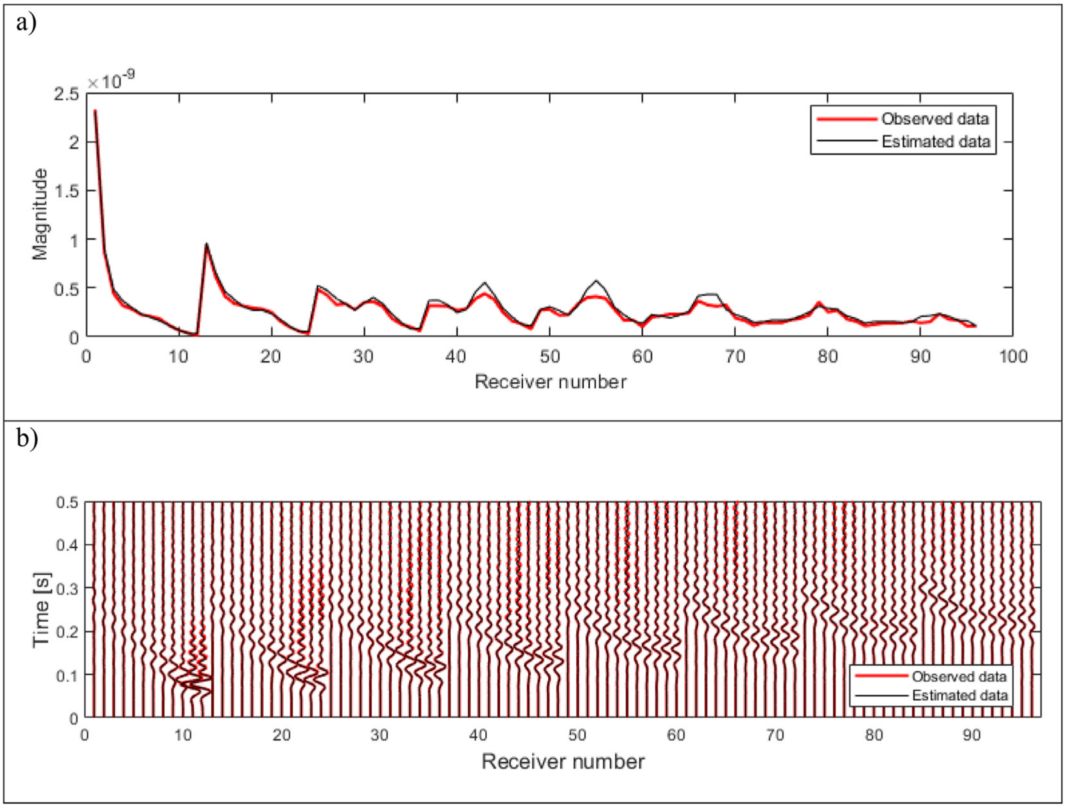

Fig. 4. Synthetic experiment waveform comparison for a sample shot (Fig. 1) at all 96 receivers: a) frequency-domain at 25 Hz with the magnitude calculated from both real and imaginary parts of the transformed waveform data, b) time-domain waveforms filtered through a bandwidth of 5–35 Hz.

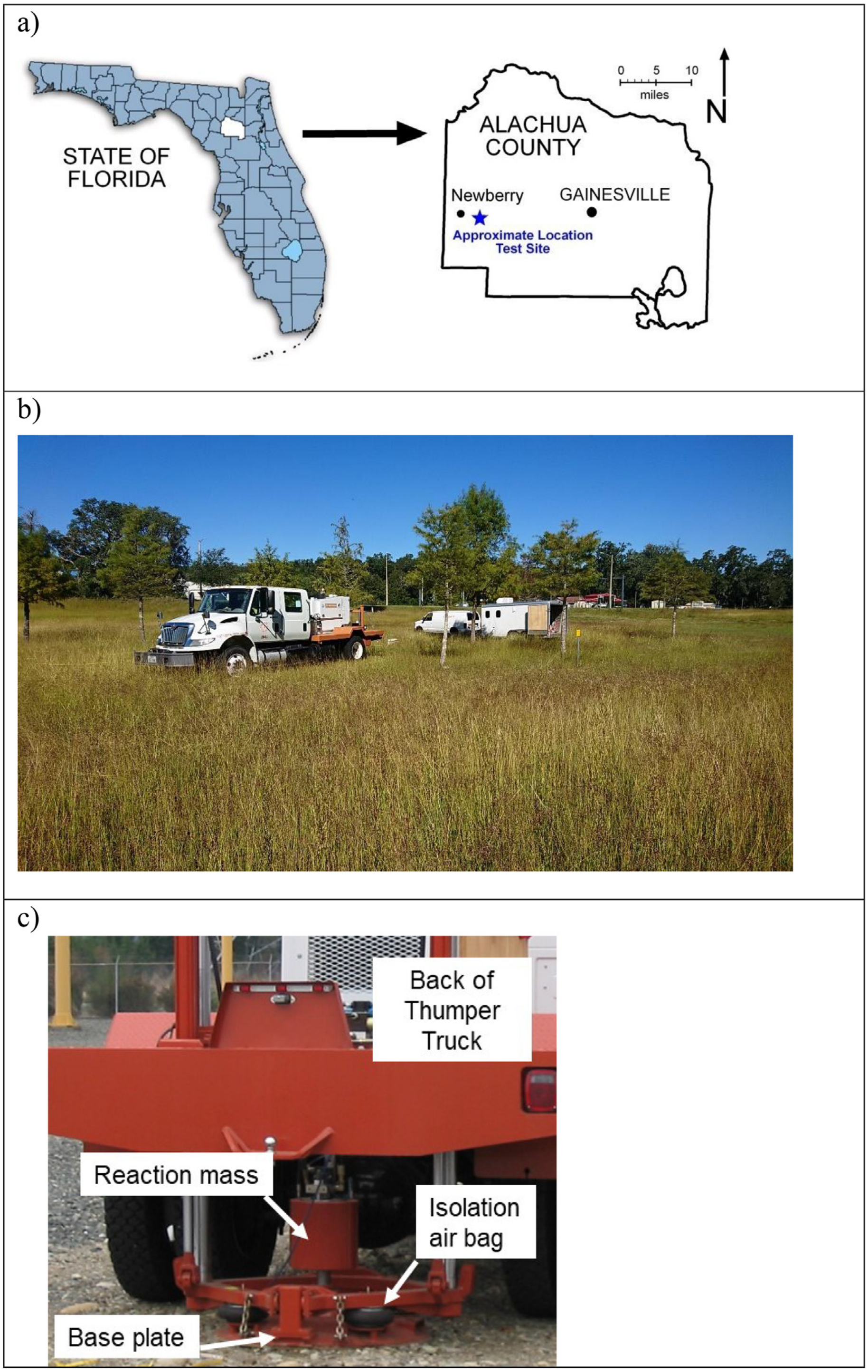

Fig. 5. Field experiment: a) site location and b) photograph of the mobile shaker truck named Thumper, and c) Thumper shaker source.

and the second run was at 20, 25 and 30 Hz. The lower frequencies (larger wavelengths) produce a misfit function with fewer local minima at further apart, thus require a less detailed initial model to get to the neighborhood of the global minimum (Bunks et al., 1995). With the selected central and adjacent frequencies, the two runs covered a wide frequency range from 12 to 30 Hz, typically used for site characterization at engineering scales.

The first run began on a 1D initial model (Fig. 2b). *Vs* linearly increased from 300 m/s (velocity of top layer) on the top (0-m depth) to 600 m/s (velocity of the half space) at the bottom (18-m depth), and *Vp* is twice that of *Vs*. This 1D initial model can be estimated via a spectral analysis as shown in the field experiment later. The second run was conducted using the inverted result from the first run as the input model. *Vs* and Vp of cells were updated simultaneously during the inversion analysis (model **m** in Eq. 4). The analysis was set to stop if the change of the least-squares errors at two consecutive iterations is less than 1%, or the preset number of iterations (20) is reached. The first and second runs stopped after 20 and 12 iterations, respectively. It took about 28 h in total on a desktop computer with 32 cores of 3.46 GHz and 256 GB RAM.

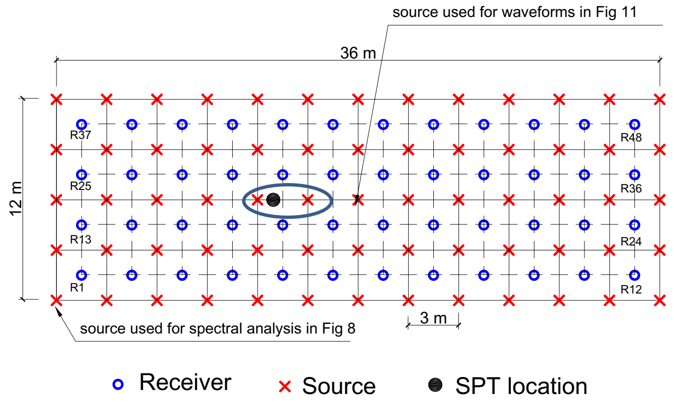

Fig. 6. Test configuration used for the field experiment on top of a known void (general location shown as elipse). Receiver numbers are shown as R1 to R48.

The least-squares errors of both inversion runs are normalized and shown in Fig. 3. The error decreased from 1.0 to 0.11 during the first run, and further during the second run. Shown in Fig. 4a is the frequency-domain waveform comparison at the central frequency of the second inversion run (25 Hz) for the first shot at all 96 receivers. The observed and estimated data are associated with the true model and the final inverted model, respectively. Apparently, there is a good agreement between the observed and estimated data. There is some discrepancy in waveform magnitudes at receivers near the void. It is mostly due to the scattered components from the sharp material contrast at the void boundary that the inversion does not fully capture due to smoothness generated by the regularization. Shown in Fig. 4b is the waveform comparison in the time-domain, where waveforms are filtered through a bandwidth of 5–35 Hz. The observed and estimated waveforms match well, suggesting that the 1-D initial model is sufficient. Interestingly, matching only a few representative frequency components leads to matching of waveforms for the entire bandwidth.

The final inverted result from the second inversion run is shown in Fig. 2c, which is similar to the true model (Fig. 2a) for both *Vs* and *Vp* profiles. The two variable layers are well characterized. The location and size of the void are recovered. For better comparison, the true, initial, and inverted values of *Vs* and *Vp* for the vertical profile at the void center are shown in the Fig. 2d. The *Vs* and *Vp* changed substantially during inversion from the initial values, and the inverted values agrees with those of the true model. There is some difference between the true and inverted values, which is mostly due to model smoothness caused by the regularization. Nevertheless, the synthetic result suggests that the presented 3D GN-FWI algorithm works well in the combined time-frequency domain. Only a few representative frequency components are needed for the waveform analysis to recover the complex model with variable layers and a void.

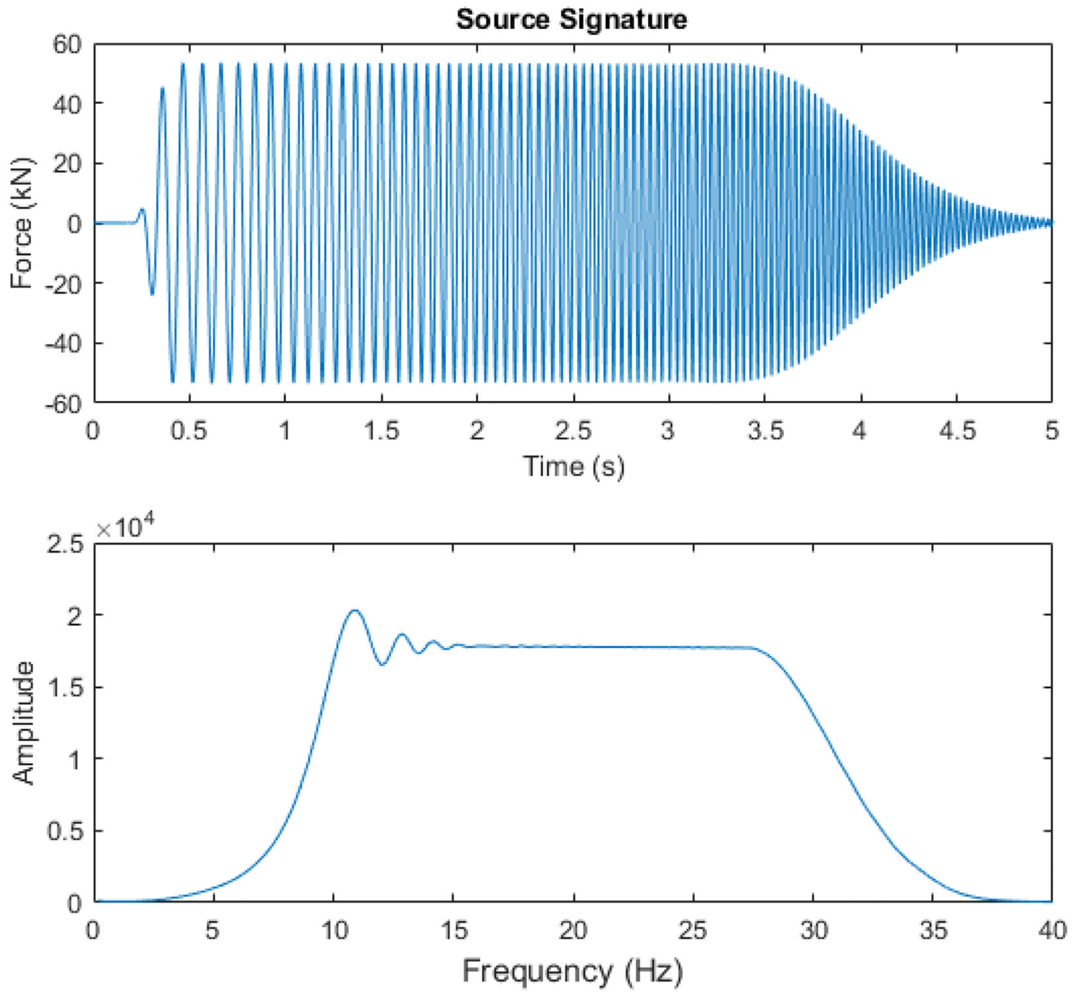

Fig. 7. Chirp source in the time-domain (top) and the coresponding spectrum (bottom).

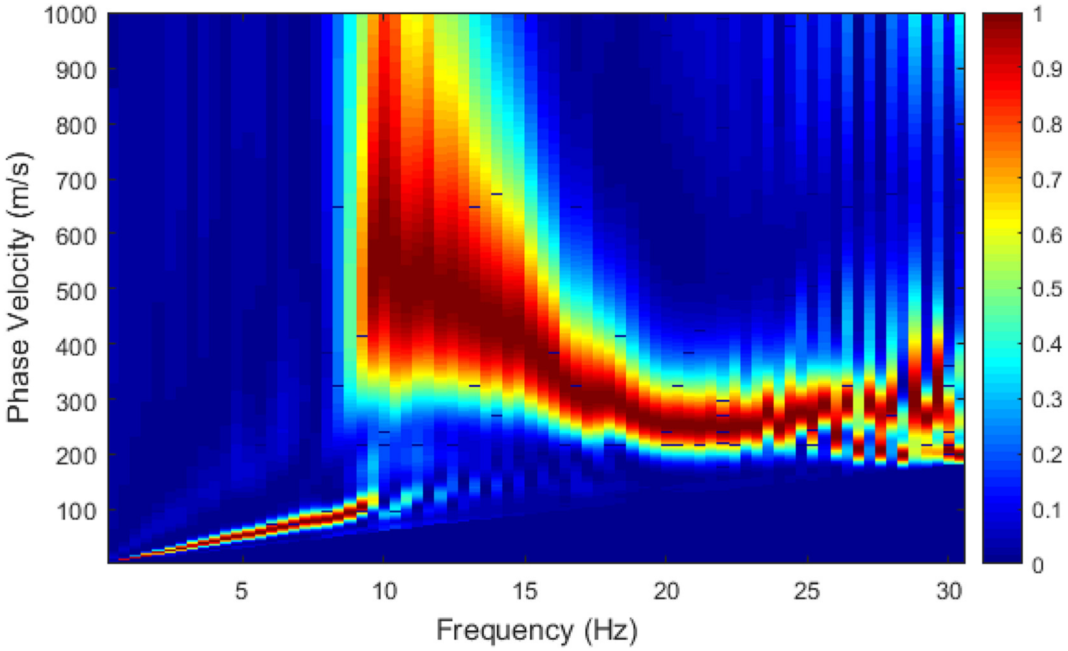

Fig. 8. Field experiment: spectral analysis of measured data for one sample shot and one line of 12 geophones.

5. Application to field data

The 3D GN-FWI method was then used for a field experiment at a retention pond in Newberry, Florida, USA (Fig. 5a). The test site consists of medium dense, fine sand and silt underlain by highly variable limestone. The top of limestone varies from 2- to 10-m in depth (Tran and Hiltunen, 2011). The seismic test area (Fig. 6) contains a known void, which was identified by a 2D FWI method and verified by an invasive SPT (Tran et al., 2013). The void is at 3.5 to 6.5 m depth with the general location shown as the ellipse in Fig. 6. The seismic experiment was conducted using 48 receivers and 65 shots located in 2D grids on the ground surface (Fig. 6). The receiver and source grids were 4 × 12 and 5 × 13, respectively, both at 3 m spacing. Seismic wavefields were created by a Thumper shaker (Fig. 5b and c) (Stokoe et al., 2017) available at the Natural Hazards Engineering Research Infrastructure equipment facility at the University of Texas at Austin (NHERI@UTexas), and recorded by 48 4.5-Hz vertical geophones simultaneously for each source location. For consistent waveform magnitudes at individual frequencies required for the presented frequency-domain inversion, the shaker induced a chirp source to generate wavefields at individual frequencies in the order of increasing frequencies.

Shown in Fig. 7 is a sample recorded source signature from field experiment in the time-domain (top) and its corresponding spectrum with the dominant frequencies from 10 to 30 Hz (bottom). It is noted that the recorded source signature (Fig. 7) was first used for the forward simulation during inversion, but there were significant inversion artifacts near the source locations that may be due to source/receiver coupling or cross-talking. Thus, we instead used estimated source signatures during inversion. The source signatures were estimated for individual source locations at the beginning of each iteration as detailed in Tran and Luke (2017), and then used for the forward simulation.

Shown in Fig. 8 is the spectral analysis of field data from the first shot (Fig. 4) recorded by a line of 12 geophones (R1 to R12). Wave energy is mostly from the active-source surface waves (narrow band from 10 to 30 Hz), together with ambient traffic noise from the nearby road (less than 10 Hz). The discontinuity in the band above 25 Hz is mostly due to spatial aliasing (*e.g.*, too coarse receiver spacing). Phase wave velocities are approximately from 300 to 600 m/s at the frequency range of 10 to 30 Hz. Assuming *Vs* of 600 m/s for the half space, a basic initial model (Fig. 9a) was established with *Vs* linearly increased with depth from 300 m/s (top layer velocity) to 600 m/s (the half space velocity). The depth of model is 18 m, as a half of the longer dimension of test area. *Vp* was calculated from *Vs* and a homogeneous Poisson's ratio of 1/3, which is a characteristic value from 1/4 to 1/2 for general soil/rock. The mass density of 1800 kg/m^3 was assumed as a typical value for both soil and limestone for the entire domain, and fixed during inversion analysis. As the dominated Rayleigh waves in measured data are not sensitive to the material density, it is difficult to extract the density from the waveform analysis.

Similar to the synthetic analysis, two inversion runs were conducted. The first run at 12, 15, and 18 Hz started with the initial model (Fig. 9a). The second run at 20, 25, and 30 Hz continued from the first run result as the input model. To account for wave attenuation in the field, the estimated data generated from the elastic forward solver was corrected by an offset dependent factor $y(r) = Ar^{\alpha}$, where r is the source-receiver distance. Parameters A and α are determined through an iterative inversion process to minimize the energy of the waveform residuals. These parameters are determined at the beginning of each inversion run, and kept constant for each run. It is noted that the factor $y(r)$ represents an average attenuation of the wavefield (both body and surface waves) over the entire test area.

The 18 × 36 × 12 m (depth × length × width) medium was discretized into 0.75 × 0.75 × 0.75 m cells. The cell size of 0.75 m was chosen as a quarter of the geophone/shot spacing (3 m) for convenience of assigning shots and receivers to numerical nodes. It is noted that the grid spacing of 0.75 m allows wave simulation up to 30 Hz with at least 5 grid points per wavelength for most of the medium (except void locations). Due to the limited computer RAM, we decided to accept some numerical dispersion at void locations, instead of using smaller cells. *Vs* and *Vp* of cells (model $\mathbf{m}$) were updated iteratively during analysis via Eq. 4. The two runs took about 32 h in total on the same computer used for the synthetic experiment.

Fig. 10 shows the normalized least-squares errors of the two inversion runs, with 20 iterations for the first run and 12 iterations for the second run. The error reduced from 1.0 at the first iteration to 0.68 at

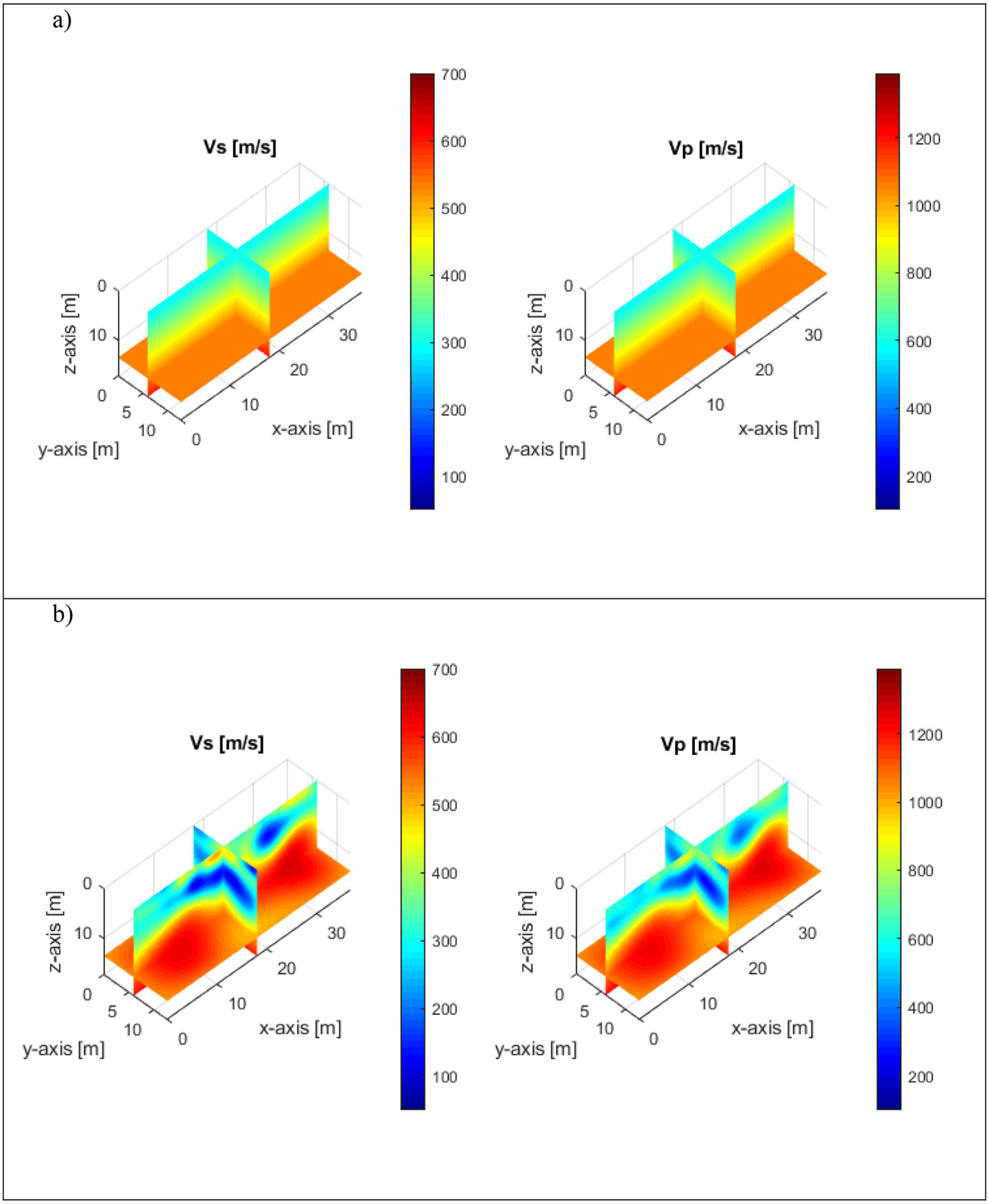

Fig. 9. Field experiment: distribution of V_S and V_P (m/s): a) initial model used at the beginning of inversion, and b) final inverted model at 25 Hz central frequency.

the final iteration (iteration 32). Shown in Fig. 11 is a comparison of observed and estimated data for a sample shot in the frequency-domain (a) and in the time-domain (b). The observed and estimated waveform data relatively match well for most channels. No cycle skiping (matching of wrong peaks) is seen in the time-domain (Fig. 11 b); suggesting the sufficency of the 1D initial model.

The final inverted results are shown in Fig. 9b. *Vs* profile (Fig. 9b, left) consists of a soft layer (*Vs* ~ 150–300 m/s), underlain by a stiff layer (*Vs* ~ 500–700 m/s). There are two buried low-velocity zones, one with *Vs* ~ 40–100 m/s at about 5-m depth near the center of the medium, and one with *Vs* ~ 70–120 m/s at about 4-m depth near distance x = 26 m. The *Vp* profile (Fig. 9b, right) is consistent with the *Vs* profile, including the softer and stiffer layers, and the two low-velocity anomalies. As identified from invasive SPT samples, the soft and stiff layers are fine sand with silt and weathered limestone, respectively.

For better viewing of subsurface features, Fig. 12 presents 3D rendering of the final inverted *Vs* and *Vp* profiles. In the *Vs* image, cells with *Vs* < 120 m/s (low-velocity anomalies) or *Vs* > 500 m/s (limestone)

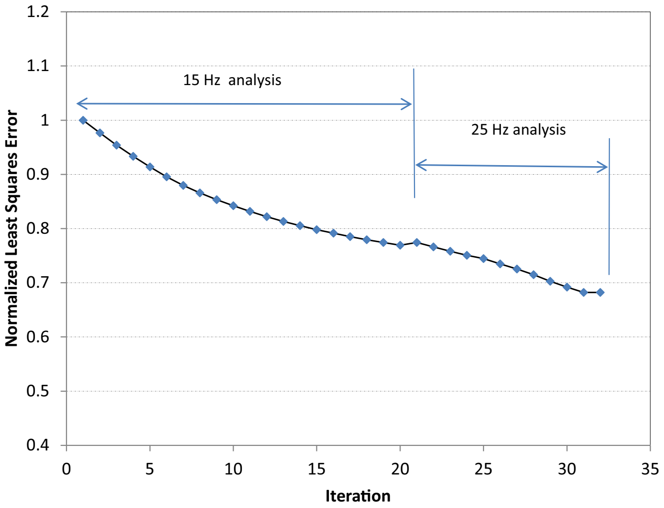

Fig. 10. Field experiment: normalized least squares error *versus* the inversion iteration number for both inversion runs at 15 Hz and 25 Hz central frequencies. The error defines the degree of match between the estimated and observed waveforms during the inversion analysis.

are shown, whereas cells with 120 m/s < *Vs* < 500 m/s are made to be transparent. Similarly, cells with *Vp* < 400 m/s (low-velocity anomalies) and *Vp* > 1000 m/s (limestone) are shown in the *Vp* image. Two low-velocity anomalies and variable limestone surface are clearly displayed in both *Vs* and *Vp* images.

Comparison of the inverted *Vs* and *Vp* images with the invasive SPT tests are shown in Fig. 13. The inverted *Vs* and *Vp* images are extracted from the slice at y = 6 m (middle of the medium). The location of the SPT test and resulting N-values are also shown in the figure. The SPT results agree well with the inverted *Vs* and *Vp* images. One of the anomalies identified in the *Vs* image is confirmed by the SPT tests. The SPT-N values are zero (air) or near zero (raveled soil) between 3.5 and 6.5 m below ground surface. The SPT ended at the top of limestone at 7 m depth, which is also consistent with the *Vs* value more than 500 m/s at that depth. With *Vs* ~ 70–120 m/s, the second anomaly at distance x = 26 m is thought to be a soft/weak soil zone, or a void filled with raveled soil/limestone. More invasive tests are required to verify the second anomaly and variable depth of the limestone layer.

6. Conclusion

A time-frequency 3D-GN FWI method is presented for anomaly detection at engineering scales. The method consist of a time-domain 3D elastic solver for the forward wave simulation, and a frequency-domain Gauss-Newton inversion for extraction of subsurface structures. The advantages of this combined time-frequency approach include that wavefields are simulated at multiple frequencies simultaneously without an inverse matrix solver, and only a few frequency components are stored for each inversion analysis to significantly reduce the

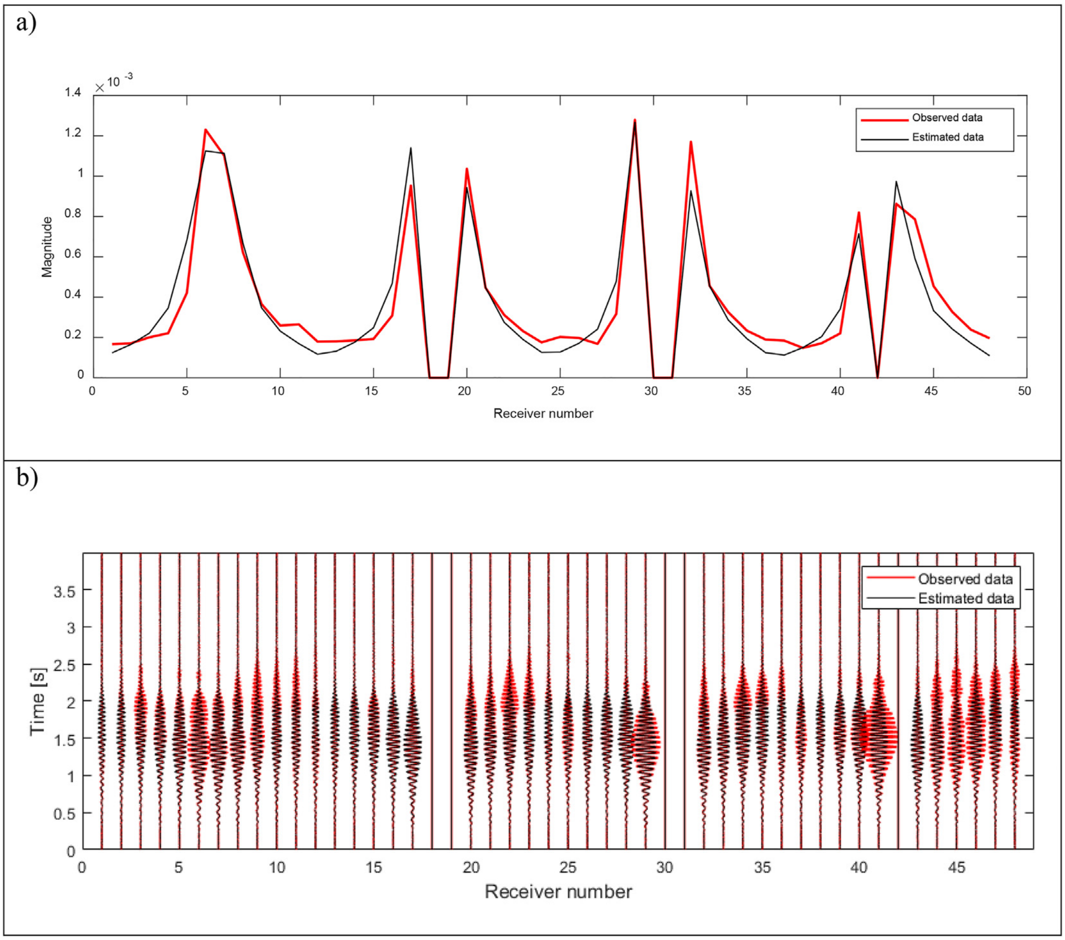

Fig. 11. Field experiment: waveform comparison for a sample shot at the middle of test area in the frequency-domain at 15 Hz (a) and the time-domain (b). Poor signals from channels near the source are removed from analysis.

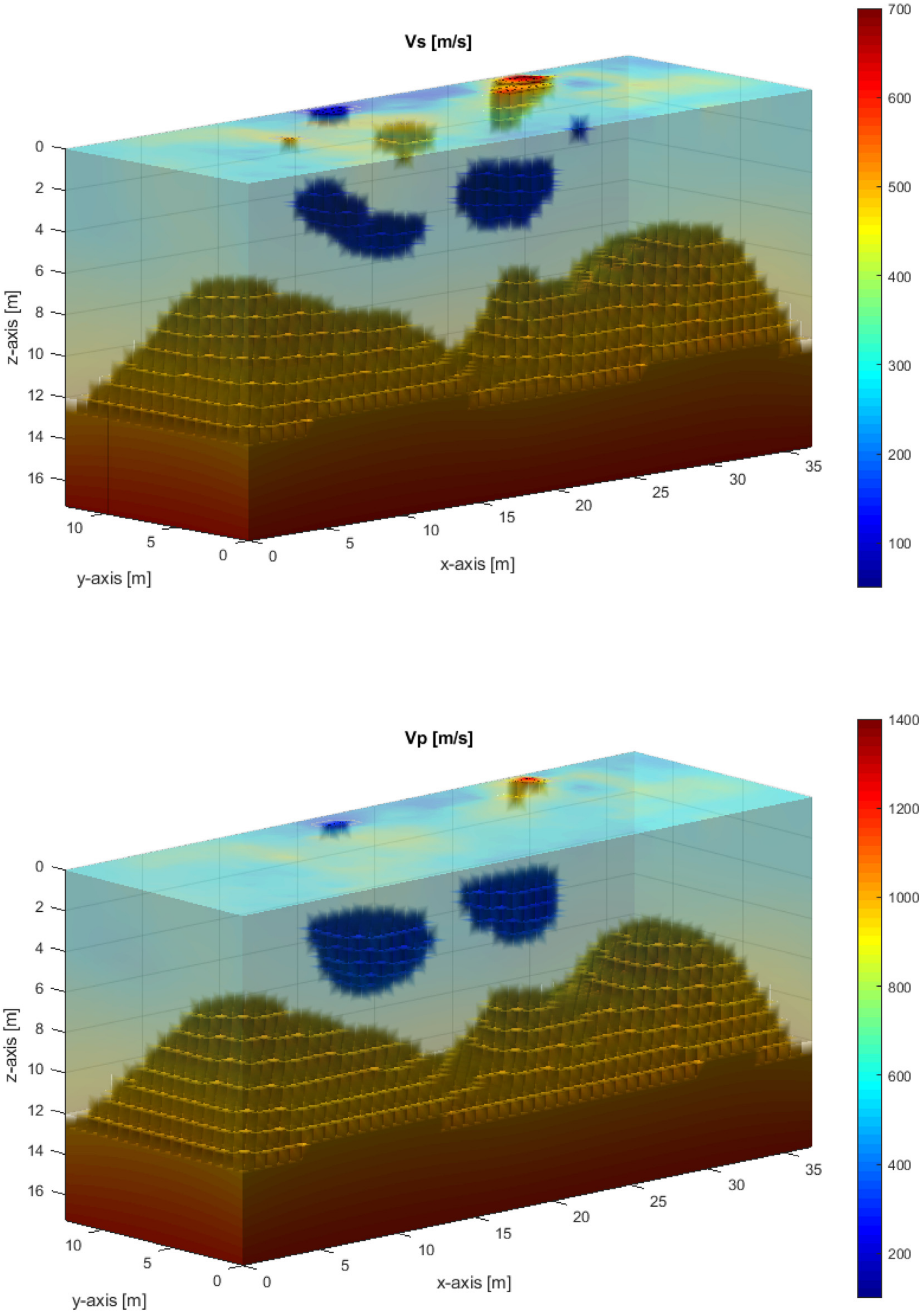

Fig. 12. 3D rendering of *Vs* and *Vp* profiles, where two low-velocity anomalies and variable limestone are clearly shown.

required computer RAM. Applied on synthetic and field experiments, the presented 3D-GN FWI method showed the excellent capabilities in detecting buried anomalies and characterizing variable soil/rock layers. The field seismic results well agree with invasive standard penetration test (SPT) N-values, including the depth of bedrock and identification of a buried void.

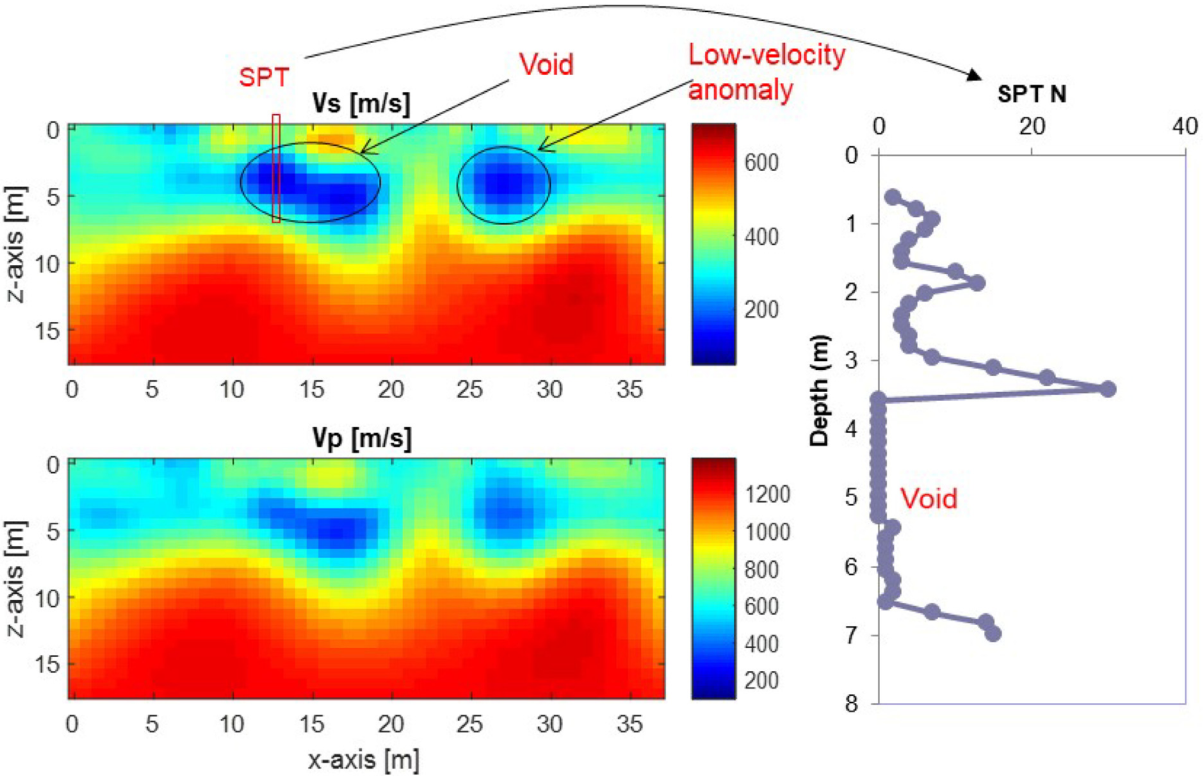

Fig. 13. Comparison of FWI seismic and invasive SPT. The inverted *Vs* and SPT results both show a void at 3.5–6.5 m depth and top of bedrock at about 7 m depth.

Author contributions

Khiem T. Tran performed writing – original draft, conceptualization, methodology, funding acquisition,

Trung Dung Nguyen performed writing – original draft, methodology, formal analysis,

Dennis R. Hiltunen performed writing – review and editing, methodology, data curation, validation,

Kenneth Stokoe and Farnyuh Menq performed writing – review and editing, data curation, validation, funding acquisition.

Declaration of Competing Interest

The authors declare that they have no known competing financial interests or personal relationships that could have appeared to influence the work reported in this paper.

Acknowledgments

The National Science Foundation financially supports of this study *via* grants CMMI-1637557, CMMI-1850696, and CMMI-1520808. We thank Florida Department of Transportation for providing access to the test site and the SPT data.

References

Pérez Solano, C., Plessix, R., 2019. Velocity model building with enhanced shallow resolution using elastic waveform inversion – An example from onshore Oman. Geophysics 84 (6), R989.

Akcelik, V., Biros, G., Ghattas, O., 2002. Parallel Multiscale Gauss-Newton-Krylov Methods for Inverse Wave Propagation, Supercomputing, ACM/IEEE 2002 Conference (2002) (41pp).

Borisov, D., Modrak, R., Gao, F., Tromp, J., 2017. 3D elastic full-waveform inversion of surface waves in the presence of irregular topography using an envelope-based misfit function. Geophysics 83 (1), R1–R11.

Prieux, V., Brossier, R., Operto, S., Virieux, J., 2013. Multiparameter full waveform inversion of multicomponent ocean-bottom-cable data from the Valhall field. Part 2: Imaging compressive-wave and shear-wave velocities. Geophys. J. Int. 194, 1665–1681.

Bunks, C., Saleck, F.M., Zaleski, S., Chavent, G., 1995. Multiscale seismic waveform inversion. Geophysics 60, 1457–1473.

Butzer, S., Kurzmann, A., Bohlen, T., 2013. 3D elastic full-waveform inversion of small-scale heterogeneities in transmission geometry. Geophys. Prospect. 2013 (61), 1238–1251.

Epanomeritakis, I., Akcelik, V., Ghattas, O., Bielak, J., 2008. A Newton-CG method for large-scale three-dimensional elastic full waveform seismic inversion. Inverse Problems 24, 26.

Fathi, A., Poursartip, B., Stokoe, K.H., Kallivokas, L., 2016. Three-dimensional P-and S-wave velocity profiling of geotechnical sites using full-waveform inversion driven by field data. Soil Dyn. Earthq. Eng. 87, 63–81.

Groos, L., Schäfer, M., Forbriger, T., Bohlen, T., 2014. The role of attenuation in 2D full-waveform inversion of shallow-seismic body and Rayleigh waves. Geophysics 79 (6), R247–R261.

Kamatitsch, D., Martin, R., 2007. An unsplit convolutional perfectly matched layer improved at grazing incidence for the seismic wave equation. Geophysics 72 (5), SM155–SM167.

Marjanovíc, M., Plessix, R.-E., Stopin, A., Singh, S.C., 2019. Elastic versus acoustic 3-D full waveform inversion at the east pacific rise 9°500'N. Geophys. J. Int. 216 (3), 1497–1506.

Métivier, L., Brossier, R., Operto, S., Virieux, J., 2017. Full waveform inversion and the truncated newton method. SIAM Review 59, 153–195.

Mirzanejad, M., Tran, K.T., 2019. 3D viscoelastic full waveform inversion of seismic waves for geotechnical site investigation. Soil Dyn. Earthq. Eng. 122, 67–78.

Mora, P., Wu, Z., 2018. Elastic versus acoustic inversion for marine surveys. Geophys. J. Int. 214 (1), 596–622.

Nguyen, D.T., Tran, K.T., 2018. Site characterization with 3-D elastic full waveform tomography. Geophysics 83 (5), R389–R400.

Pan, Y., Gao, L., Bohlen, T., 2018. Time-domain full-waveform inversion of Rayleigh and love waves in presence of free-surface topography. J. Appl. Geophys. 152, 77–85.

Park, C.B., Miller, R.D., Xia, J., 1999. Multichannel analysis of surface waves. Geophysics 64 (3), 800–808.

Pérez Solano, C., Donno, D., Chauris, H., 2014. Alternative waveform inversion for surface wave analysis in 2-D media. Geophys. J. Int. 198 (3), 1359–1372.

Plessix, R.-E., Milcik, P., Rynja, H., Stopin, A., Matson, K., 2013. Multiparameter full waveform inversion: marine and land examples. Leading Edge 32 (9), 1030–1038.

Pratt, R.G., Shin, C., Hicks, G.J., 1998. Gauss-Newton and full Newton methods in frequency-space seismic waveform inversion. Geophysical Journal International 133, 341–362.

Raknes, E.B., Arntsen, B., Weibull, W., 2015. Three-dimensional elastic full waveform inversion using seismic data from the Sleipner area. Geophys. J. Int. 202, 1877–1894.

Robertsson, J.O.A., 1996. A numerical free-surface condition for elastic/viscoelastic finite-difference modeling in the presence of topography. Geophysics 61, 1921–1934.
Sedova, A., Royle, G., Hermant, O., Retailleau, M., Lambaré, G., 2017. High-resolution land full waveform inversion - a case study on a data set from the sultanate of Oman. Proceedings of the 79th International Conference and Exhibition, EAGE, Extended Abstracts. Paris, France.
Sheen, D.H., Tuncay, K., Baag, C.E., Ortoleva, P.J., 2006. Time domain Gauss–Newton seismic waveform inversion in elastic media. Geophys. J. Int. 167, 1373–1384.
Sirgue, L., Barkved, O.I., Dellinger, J., Etgen, J., Albertin, U., Kommedal, J.H., 2010. Full waveform inversion: the next leap forward in imaging at Valhall. First Break 28, 65–70.
Smith, J.A., Borisov, D., Cudney, H., Miller, R.D., Modrak, R., Moran, M., Peterie, S.L., Sloan, S.D., Tromp, J., Wang, Y., 2018. Tunnel detection at yuma proving ground, Arizona, USA — Part 2: 3D full-waveform inversion experiments. Geophysics 84 (1) (B95–B10).
Stokoe, H., Cox, B., Clayton, P., Menq, F., 2017. NHERI@UTexas Experimental Facility: Large-Scale Mobile Shakers for Natural Hazard Field Studies to Develop Resilient and Sustainable Infrastructure, 16th World Conference on Earthquake Engineering, Santiago, Chili.
Stopin, A., Plessix, R.-E., Al, Abri S., 2014. Multiparameter waveform inversion of a large wide-azimuth low-frequency land data set in Oman. Geophysics 79, WA69–WA77.
Taillandier, C., Noble, M., Chauris, H., Calandra, H., 2009. First-arrival traveltime tomography based on the adjoint-state method. Geophysics 74 (6), WCB1–WCB10.
Tran, K.T., Hiltunen, D.R., 2011. Inversion of first-arrival time using simulated annealing. Journal of Environmental and Engineering Geophysics 16, 25–35.
Tran, K.T., Hiltunen, D.R., 2012. Inversion of combined surface and borehole first-arrival time. Journal of Geotechnical and Geoenvironmental Engineering 138 (3), 272–280.
Tran, K.T., Luke, B., 2017. Full waveform tomography to resolve desert alluvium. Soil Dyn. Earthq. Eng. 9, 1–8.
Tran, K.T., Sperry, J., 2018. Application of 2-D full waveform tomography on land-streamer data for assessment of roadway subsidence. Geophysics 83 (3), EN1–EN11.
Tran, K.T., McVay, M., Faraone, M., Horhota, D., 2013. Sinkhole detection using 2-D full seismic waveform tomography. Geophysics 78 (5), 175–183.
Tran, K.T., Mirzanejad, M., McVay, M., Horhota, D., 2019. 3D time-domain Gauss-Newton full waveform inversion for near-surface site characterization. Geophys. J. Int. 217, 206–218.
Vigh, D., Kapoor, J., Moldoveanu, N., Li, H., 2011. Breakthrough acquisition and technologies for subsalt imaging. Geophysics 76 (5), WB41–WB51.
Vigh, D., Jiao, K., Watts, D., Sun, D., 2014. Elastic full-waveform inversion application using multicomponent measurements of seismic data collection. Geophysics 79 (2), R63–R77.
Vireux, J., Operto, S., 2009. An overview of full-waveform inversion in exploration geophysics. Geophysics 74 (6), WCC1–WCC26.
Virieux, J., 1986. P–SV wave propagation in heterogeneous media: velocity–stress finite-difference method. Geophysics 51 (4), 889–901.
Warner, M., Ratcliffe, A., Nangoo, T., Morgan, J., Umpleby, A., Shah, N., 2013. Anisotropic 3D full-waveform inversion. Geophysics 78 (2), R59–R80.
Wightman, W., Jalinoos, F., Sirles, P., Hanna, K., 2003. Applications of Geophysical Methods to Related Highway Problems: FHWA Technical Manual.